

Monochromatic aberrations and point-spread functions of the human eye across the visual field

Rafael Navarro, Esther Moreno, and Carlos Dorronsoro

*Instituto de Optica "Daza de Valdés," Consejo Superior de Investigaciones Científicas, Serrano 121,
28006 Madrid, Spain*

Received December 1, 1997; revised manuscript received February 17, 1998; accepted February 17, 1998

The monochromatic aberrations of the human eye along the temporal meridian are studied by a novel laser ray-tracing method. It consists of delivering a narrow laser pencil into the eye through a given point on the pupil and recording the aerial image of the retinal spot with a CCD camera. The relative displacement of this image is proportional to the geometrical aberration of the ray (laser pencil) at the retina. We scanned the pupils of four observers in steps of 1 mm (effective diameter, 6.7 mm) and for five field angles (0°, 5°, 10°, 20°, and 40°). In addition, the aerial image for each chief ray is a low-pass-filtered version of the retinal point-spread function corresponding to a fully dilated pupil. The resulting spot diagrams, displaying the distribution of ray aberrations, are highly correlated with these point-spread functions. We have estimated the wave-front error by fitting Zernike polynomials (up to the fifth order). Despite the large variation found among observers, the overall rms wave-front error is relatively homogeneous. At the fovea, the average rms value was 1.49 μm when the second-order terms (defocus and astigmatism) were considered; this was reduced to 0.45 μm when the second-order terms were ignored. The rms values increase slowly, in a roughly linear fashion with eccentricity, such that at 40° they are approximately double. These results are consistent with previous findings on the off-axis optical quality of the eye. © 1998 Optical Society of America [S0740-3232(98)00109-4] *OCIS codes:* 330.5370, 330.0330.

1. INTRODUCTION

The overall monochromatic wave-front aberration of the eye has often been measured for central, foveal vision by both subjective (different spatially resolved refractometers¹⁻⁴ or the Hartmann test⁵) and objective methods (Foucault knife edge,⁶ Hartmann test,⁷ Hartmann-Shack,^{8,9} or laser ray tracing¹⁰). However, little attention has been paid to eccentric visual fields, for which only studies of refraction, defocus, and astigmatism¹¹⁻¹³ and related field curvature¹⁴ have been reported. Other studies have focused on the overall image quality, such as line-spread¹⁵ and modulation transfer functions^{16,17} (MTF's). Our goal in this study was to obtain experimental data on the off-axis overall monochromatic aberration of the eye, for which there is a marked lack of experimental data. We believe that this kind of study is very important for several reasons. Recent evidence, for instance, in progressive ophthalmic lens wearers, suggests that, although retinal resolution in the periphery is much poorer than in the fovea, an excessively bad off-axis optical quality seems to impair performance in some tasks related to peripheral vision (see, for instance, Ref. 18). On the other hand, experimental studies on the off-axis image quality show that the decline with eccentricity in the MTF is much slower than in retinal sampling.^{16,17} These findings indicate that, compared with a conventional lens, the eye shows a poor optical quality at the fovea (on axis) but a surprisingly high homogeneity with eccentricity. This is compatible with very-wide-angle lens design, but such optical design seems to yield a puzzling mismatch with the highly inhomogeneous structure of the retina.

Study of the off-axis aberrations of the eye could perhaps lead to a better understanding of the functionality of peripheral vision.

Among the different methods mentioned above, most subjective approaches would hardly work in the periphery, since visual acuity away from the fovea drops rapidly, causing a subsequent drop in the accuracy of the subjective judgments. Objective methods are well suited for peripheral measurements, but a potential drawback is that most of them consist of delivering some light into the retina (first pass) and then analyzing the outgoing beam, after a second pass, outside the eye. Therefore one has to assume reversibility between incoming and outgoing beams. [A necessary condition is that the point-spread function (PSF) has to be smaller than the isoplanatic patch, which could potentially fail for large aberrations associated with large pupils and eccentricities.] For this reason we have adopted a novel sequential laser ray-tracing technique,¹⁰ in which we measure the relative angular coordinates at the retina ($\Delta x'$, $\Delta y'$; i.e., the transverse geometrical aberration) of the spot formed by a laser pencil passing through a given point with coordinates (ξ , η) at the pupil plane. Experimental results obtained in the right eyes of four observers, for eccentricities between 0° and 40°, are consistent with previous findings that optical quality decreases slowly with visual field. This suggests that, at the fovea, tilts, decentering, lack of rotational symmetry of cornea and lens, and other potential defects tend to cause a deterioration in optical quality that is of the same order of magnitude as that associated with a lens working off axis.

2. METHODS

The principle of the laser ray-tracing method has already been presented in Ref. 10, and the apparatus is schematically illustrated in Fig. 1. A green He-Ne laser, mounted on two computer-controlled motor-driven X and Y micropositioners, delivers monochromatic ($\lambda = 543$ nm) light pencils passing through the desired pupil coordinates (ξ, η). A set of neutral-density (ND) filters reduces the output intensity to a safe level. Typical intensities at the cornea for foveal exposures are $\sim 2 \mu\text{W}$, roughly 3 log units below safety standards¹⁹ for our 200-ms exposures. (Higher intensities, up to 10–20 μW , are used for the highest eccentricity, 40° .) A computer-controlled shutter attached to the laser head moves with it. A beam-splitter pellicle directs the unexpanded laser pencil (~ 0.7 -mm effective diameter) toward the observer's eye. (The light trap absorbs the transmitted part of the beam.) The light reflected off the retina passes again through both the optical system of the eye and the beam splitter and is imaged onto a cooled slow-scan CCD camera with an $f = 105$ mm photographic objective. The fixation target, consisting of a small light-emitting diode, is placed on an auxiliary optical bench for eccentricities between 5° and 40° . For foveal measurements the light-emitting diode is viewed through a second beam splitter. When the beam passes through the center of the pupil, acting as the chief ray, it intersects the retina at a given point O . The outgoing beam forms an aerial image O' of the retinal spot O on the CCD. However, when we displace the laser so that the light pencil enters the eye through an eccentric point on the pupil, then the ray is

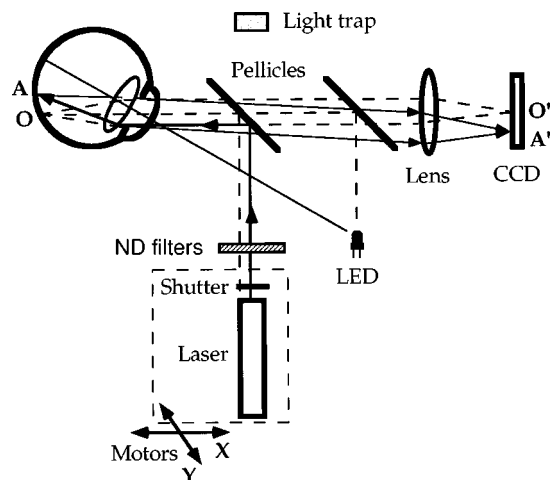


Fig. 1. Schematic diagram of the experimental setup and of the operating principle of the laser ray-tracing method. A green He-Ne laser is mounted, with a shutter attached, on an XY motor-driven micropositioning stage. The unexpanded beam is attenuated by neutral-density (ND) filters and enters the eye after reflection on a pellicle beam splitter. After reflection off the retina, a photographic objective (Lens) forms an aerial image on the CCD. The fixation target is a light-emitting diode (LED). It can be viewed either through a second beam splitter for foveal measurements or directly for off-axis measurements. When the laser pencil enters through an eccentric position of the pupil, it intersects the retina at point A . The chief ray (dashed curves) passing through the center of the pupil goes to point O . The lens of the CCD camera forms the aerial images A' and O' of these spots.

aberrated and goes to a point A , generally different from O . In this case the aerial image is displaced to point A' , which is the geometrical image of A .

This laser method has been tested with both real and artificial eyes. In the former case, foveal data have already been presented and discussed elsewhere.¹⁰ We have also made several test experiments with an artificial eye. In these experiments, second-order aberrations (defocus and astigmatism) were artificially generated with a set of trial lenses of known spherical or cylindrical powers. Then we performed ray-tracing measurements, fitting Zernike polynomials (see Section 3 below), and compared the resulting values of the measured defocus and/or astigmatism to the nominal values of the trial lenses. Differences between nominal and measured values, in diopters, were less than 7%.

Four observers ranging in age from 24 to 40 years participated in the present study, with their eyes naked [two males (CD, age 25, and RN, age 40) and two females (EM and FB, both age 24)]. For all of them the right eye was measured. Cycloplegia and dilation were achieved by instillation of 2 drops of 1% cyclopentolate, administered 5 min apart. An additional drop was given after every hour to ensure continued complete cycloplegia. Observers were fixed on a bite-bar mounted on an XY micropositioner. Careful centering of the eye's pupil was achieved both horizontally and vertically, localizing the four (up, down, left, and right) edges of the pupil. For this purpose the laser pencil, placed at coordinates $X = Y = 0$ (optical axis), was further attenuated with additional filters (optical density ≈ 3.5). Then the shutter was opened, and the observer moved the bite bar so that the beam intersected the edge of his or her pupil. At this point there is an abrupt change in the intensity entering the eye. Observers were instructed to find the position of maximum change in perceived intensity. This procedure was repeated three times, and the mean was computed. Then the eye was placed so that the laser beam passed through its pupil center, $\xi = \eta = 0$. After centering, a forehead rest with three independent adjustable parts (left, center, and right) was adjusted to the observer's head for additional rigidity of fixation. When measuring off axis, we displaced the pupil horizontally to compensate for the offset produced by the rotation of the eye. Offsets were calculated assuming that the eye's center of rotation is 9 mm behind the pupil.²⁰ Nevertheless, for large eccentricities (20° and 40°) we verified alignment experimentally, again localizing the edges of the pupil and bringing its center to coincide with that of the artificial pupil, to avoid potential failure of that assumption.

To trace a ray the laser was positioned so that the beam passed through the pupil at the desired position (ξ, η), the shutter was opened for 0.2 s, and the aerial image was recorded on the CCD. We adjusted the laser intensity by means of the ND filters in order to match the dynamic range of the CCD while carefully avoiding saturation. This exposure time was smaller than typical reflex reaction time, which is ~ 250 ms. This is usually sufficient to avoid involuntary saccadic movements of the observer, who sometimes tends to fixate toward the deflected bright input beam, while being long enough to blur, at least partially, speckle noise. In this study we scanned the pupil

by tracing rays in steps $\Delta\xi = \Delta\eta = 1$ mm, from -3 to $+3$ in both axes. For a circular pupil this means 37 rays (see Fig. 3 in Ref. 10). The effective pupil diameter covered with this scan is 6.7 mm (6-mm run length of scan convolved with the physical width of the laser pencil, 0.7-mm diameter). We also delivered four reference margin rays with coordinates $\xi, \eta = \pm 4$, which helped to verify the pupil position. For off-axis measurements, the horizontal coordinates of the laser beam (rays) were scaled by the cosine of the eccentricity, and hence the sampling steps were $\Delta\xi = \cos\theta, \Delta\eta = 1$ (mm) to ensure that all 37 rays passed through the now slanted pupil, regardless of the visual field angle θ . With this procedure we ensured the same sampling of the physical circular pupil independent of the slant that it may present with respect to the optical axis of the measuring system. However, the effective pupil is the projection of the circular physical one. Thus, after collecting and processing data, we have to take into account the varying rectangular (field-angle-dependent) sampling practiced. Apart from maintaining a constant number of rays, this procedure enables us to apply a convenient mathematical artifice. During the data analysis and Zernike polynomial fitting, we do not need to use explicitly the physical dimensions of the pupil sampling steps. Thus we can simply work in units of these steps, so that we always get a circle, and assign physical units only at the end of the process, transforming the numerical circle with no dimensions into an ellipse with physical dimension. This is useful to estimate the wave aberration, since Zernike polynomials form a complete basis to represent a function with a circular support of unit radius.²¹ Consequently, we adopted canonical pupil coordinates, normalized by the pupil radius in further data analysis. The wave aberration is given below in a mathematical circle of unit radius. To pass from canonical coordinates to physical units, both axes have to be scaled by $3.35 \cos\theta$ mm and 3.35 mm, respectively.

The geometrical transverse aberrations ($\Delta x', \Delta y'$) at the image plane (retina) are estimated, by the standard procedure of computing the displacement of the centroid in the aerial image with respect to that of the chief ray. The image of the retina formed on the CCD was inverted, but the CCD itself was inverted with respect to the retina since they were looking at each other, thus compensating for the optical inversion. Thus the X axis was oriented equally in both the CCD and the retina. In addition, the CCD was inverted in the Y axis, so its optical inversion was compensated for in both axes. To compute the centroid, only points in the image whose intensities were clearly above the background noise levels were considered. For this purpose, we computed the intensity histogram for each image (256×256 pixels) and took the mode M and the standard deviation σ as rough (over)estimates of the background and noise levels, respectively. Then we applied a threshold²² $T = M + 3\sigma$ to consider only pixels with a high signal-to-noise ratio. The relationship between geometrical and wave aberration (under the linear approximation) is given by²³

$$\Delta x' = \frac{1}{R_p} \frac{\partial W(\bar{\xi}, \bar{\eta})}{\partial \bar{\xi}}, \quad \Delta y' = \frac{1}{R_p} \frac{\partial W(\bar{\xi}, \bar{\eta})}{\partial \bar{\eta}}, \quad (1)$$

where $\bar{\xi} = \xi/R_p$ and $\bar{\eta} = \eta/R_p$ are canonical coordinates normalized to the pupil radius R_p (in mm); $\Delta x'$ and $\Delta y'$ are angular coordinates (in mrad) at the retinal plane; and W is the wave aberration (in μm). Since a direct numerical integration with noisy data is difficult, the standard procedure is to integrate by approximating the wave aberration by a Zernike polynomial Z_i expansion within the circle of unit radius

$$W(\bar{\xi}, \bar{\eta}) = \sum_i C_i Z_i(\bar{\xi}, \bar{\eta}), \quad (2)$$

and then to fit its partial derivatives to find the coefficients C_i (given in μm). Here we have considered a fifth-order approximation, that is, first to fifth orders, $i = 1, \dots, 20$ (in the monomial representation given in Table 13.2 of Ref. 21).

Measurements were taken at $0^\circ, 5^\circ, 10^\circ, 20^\circ$, and 40° along the temporal meridian (the side of the retina away from the optic disk). At each eccentricity we performed either three (for observers CD and FB) or four (for observers EM and RN) pupil scans.

One interesting feature of this ray-tracing method is that the aerial image corresponding to the chief ray (when the pencil passes through the center of the pupil) is the PSF of the eye convolved with a small Gaussian spot.²⁴ When the pupil is fully open this Gaussian spot is much smaller than the PSF, and therefore the aerial image is a good approximation to the (inverted) retinal PSF. We recorded these aerial images again with longer exposures (2 or 3 s, depending on the case) to reduce speckle noise. For each observer and eccentricity we took four exposures plus one background recording; then we subtracted the background from each image and took the average. These PSF estimates correspond to larger pupils (nearly 9 mm for most observers), whereas ray-tracing data correspond to 6.7-mm pupils; nevertheless, the overall shape should be similar in both cases, although the spot diagram should be smaller, and therefore it must be contained within the PSF.

3. RESULTS AND DISCUSSION

A. Spot Diagrams and Point-Spread Functions

Figure 2 shows the ray-tracing raw data for all observers, eccentricities, and series (3 or 4 depending on the subject, as explained above). Each experimental point is represented by a small dot. In the same figure, these experimental spot diagrams are compared with those obtained after Zernike polynomial least-squares fitting to estimate the wave aberration. These simulated spot diagrams (open circles) were computed as the partial derivatives of the estimated wave aberration, described by the Zernike polynomials. In this way we can visually appreciate the goodness of the fit in each case. In general, the fit is good, although in some cases such as that of FB at 10° there are a significant number of experimental dots outside the area covered by the circles. This could indicate the presence of higher-order aberrations that our fifth-order approximation cannot represent. In addition, Fig. 3 displays the aerial *one-and-a-half-pass* images, each being a rough estimate (low-pass-filtered version) of the

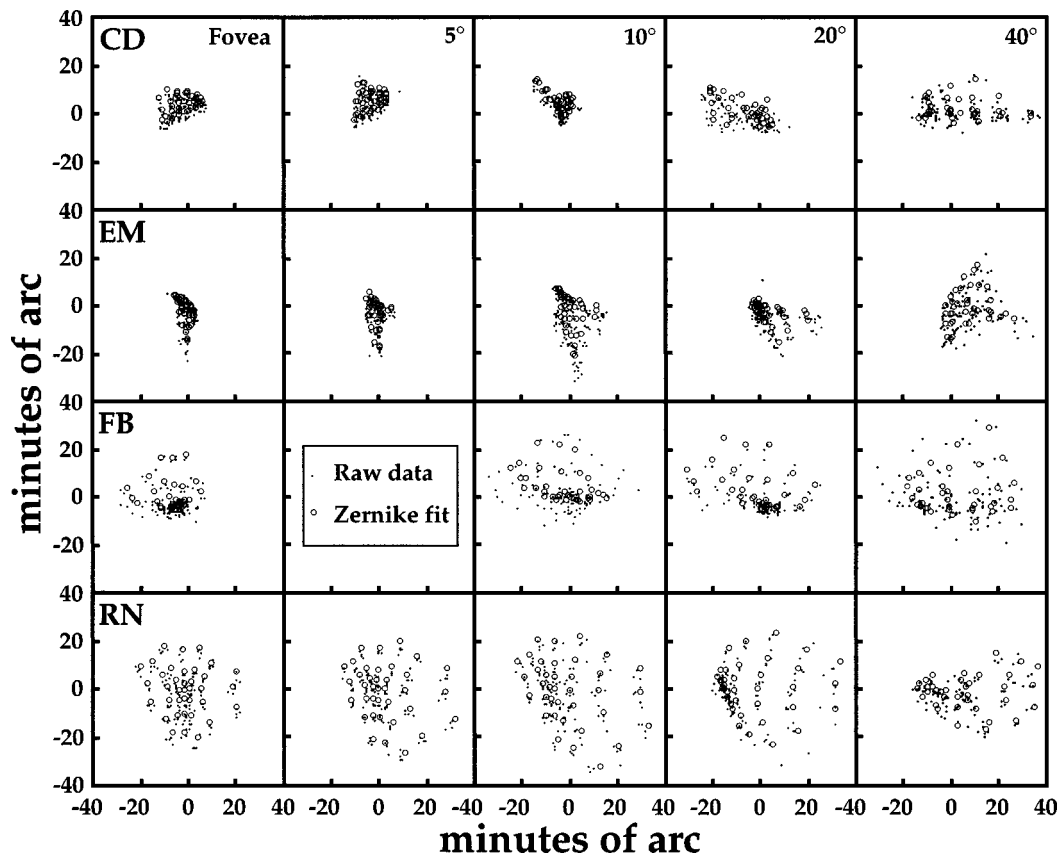


Fig. 2. Spot diagrams for our four observers at different retinal eccentricities 0°, 5°, 10°, 20°, and 40°. All the experimental data (of three or four runs, depending on the observer), represented by small dots, are included. In each diagram the open circles represent the result of Zernike polynomial fit.

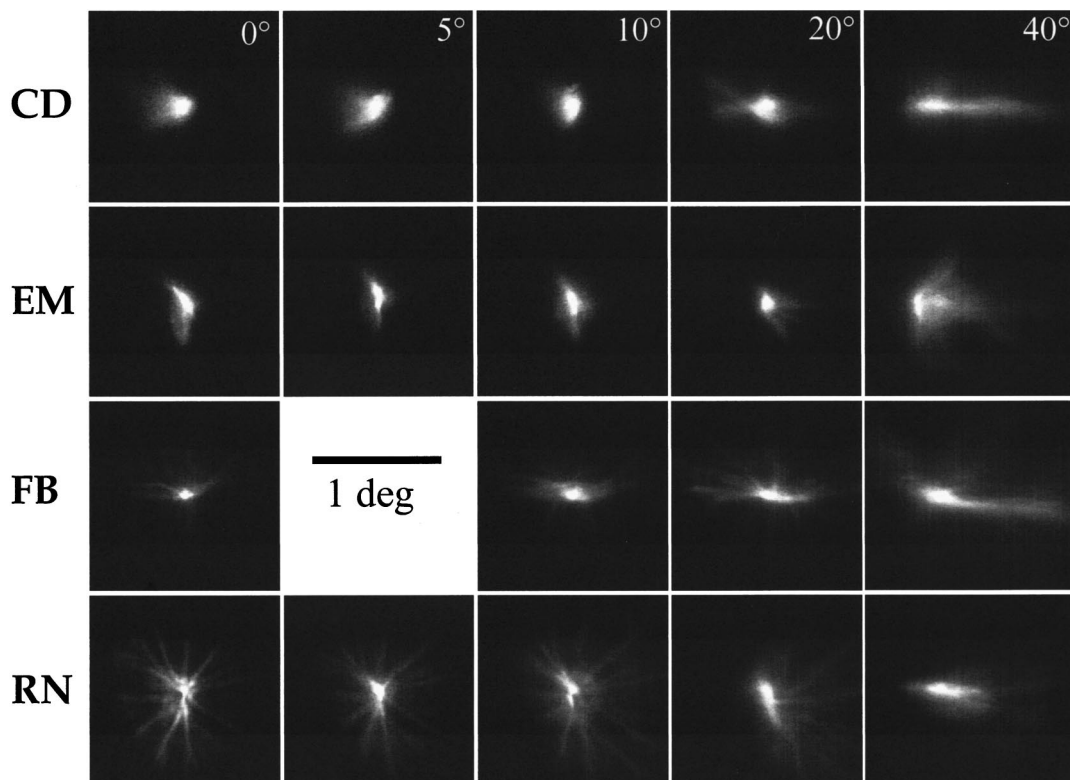


Fig. 3. Aerial images obtained by delivery of the laser pencil through the center of the pupil after reversal of both axes. These images are slightly blurred versions of the corresponding retinal PSF's.

PSF.²⁴ These aerial images simply correspond to the chief ray passing through the center of the pupil, and therefore they are the second-pass PSF's convolved by the Gaussian spot formed by the laser pencil onto the retina. The second-pass PSF is inverted with respect to the first-pass retinal one. Consequently, both axes have been reversed in Fig. 3 to permit an easier direct visual comparison with the retinal spot diagrams. In both figures we show all the experimental results, obtained at 0°, 5°, 10°, 20°, and 40°, except for those from observer FB (for this observer we did not record data at 5°). When Figs. 2 and 3 are compared, it is important to notice that the aerial images (Fig. 3) were taken through a fully dilated pupil, in the range 8.5–9 mm, depending on the observer. However, the pupil diameter in the spot diagrams (Fig. 2) is 6.7 mm. (To compare spot diagrams to diffractive PSF's we also have to consider the full width of the laser pencil, 0.7 mm, so the effective pupil is 6.7 mm.) The scale in both figures is similar but slightly different (the window size of the spot diagram is 1.333°, and it is 1.48° for the aerial images), which means that the spot diagrams are displayed with a relative higher (11%) magnification. Nevertheless, the high correlation between PSF's and spot diagrams is remarkable. One possible explanation for the fact that the spreading in the aerial images is not much larger than in the spot diagrams, in view of the different pupil diameters, could be apodization by the Stiles–Crawford effect.

One of the main differences between Figs. 2 and 3 is related to the star patterns that clearly appear for two myo-

pic observers (FB and RN) at low eccentricities. This result is consistent with previous findings that, while star patterns are clear in myopic observers, the rays become shorter or disappear for in-focus or slightly hypermetropic eyes.²⁵ These ray patterns are probably produced by fine structures (such as suture lines of the lens²⁵) and thus cannot be detected by our coarse sampling ($\Delta\xi = \Delta\eta = 1$ mm) of the pupil applied in the ray-tracing measurements. When we move from the fovea to the periphery, the pattern of change is rather similar for all four observers. The most important fact is a smooth, slow change in the shape and size of the patterns (spot diagrams and PSF's). The global effect is a slow decline in image quality (see Fig. 5 below for quantitative data). The aerial images also show a decline in contrast of features such as ray patterns, perhaps suggesting a gradual increase of light scattering. There is also a large interobserver variability, but the major contribution to this variability is that of second-order aberrations (defocus, astigmatism, and field curvature), which are discussed below.

B. Wave Aberration

Zernike coefficients, up to the fifth order, are given in Table 1 in micrometers, for one observer, EM, for all eccentricities (data for the other observers are not included here but are available on request). They were obtained by a least-squares fit of all the data from four runs, taken together, whereas we estimated the standard deviation, also included, as a measure of the variability by fitting the results of each of the four runs independently. In

Table 1. Zernike Coefficients and Their Standard Deviations (in μm), for Observer EM, for the Different Retinal Eccentricities

Zernike Coefficient	Retinal Eccentricity ^a				
	0°	5°	10°	20°	40°
Z_1	-0.26 ± 0.32	-0.30 ± 0.51	0.53 ± 0.21	2.19 ± 0.09	7.07 ± 0.78
Z_2	-1.62 ± 3.94	-2.03 ± 0.36	-2.21 ± 0.26	-2.18 ± 0.25	-0.53 ± 0.55
Z_3	0.84 ± 0.55	0.67 ± 0.15	0.86 ± 0.06	1.13 ± 0.10	2.40 ± 0.59
Z_4	-1.59 ± 0.22	-1.66 ± 0.09	-2.46 ± 0.08	-1.79 ± 0.11	1.11 ± 0.64
Z_5	-1.13 ± 0.65	-1.48 ± 0.14	-1.45 ± 0.10	0.51 ± 0.30	3.35 ± 0.48
Z_6	-0.34 ± 0.28	-0.56 ± 0.06	-0.57 ± 0.06	-0.66 ± 0.04	-0.40 ± 0.16
Z_7	-0.24 ± 0.09	-0.24 ± 0.04	0.26 ± 0.09	0.99 ± 0.05	2.68 ± 0.30
Z_8	-0.54 ± 0.44	-0.72 ± 0.02	-0.64 ± 0.11	-0.61 ± 0.06	-0.36 ± 0.19
Z_9	-0.61 ± 0.33	-0.73 ± 0.12	-0.65 ± 0.12	-0.24 ± 0.09	-0.02 ± 0.04
Z_{10}	-0.05 ± 0.26	0.20 ± 0.04	0.30 ± 0.05	0.19 ± 0.04	0.60 ± 0.19
Z_{11}	-0.09 ± 0.07	-0.12 ± 0.04	0.13 ± 0.07	0.16 ± 0.09	0.28 ± 0.07
Z_{12}	0.10 ± 0.07	0.05 ± 0.03	0.04 ± 0.02	-0.04 ± 0.02	-0.09 ± 0.04
Z_{13}	-0.02 ± 0.08	0.07 ± 0.02	0.02 ± 0.05	0.16 ± 0.07	0.12 ± 0.14
Z_{14}	-0.16 ± 0.16	-0.27 ± 0.01	-0.28 ± 0.09	-0.14 ± 0.15	0.08 ± 0.13
Z_{15}	0.07 ± 0.06	0.15 ± 0.06	0.08 ± 0.04	0.23 ± 0.04	0.22 ± 0.10
Z_{16}	-0.06 ± 0.06	-0.05 ± 0.05	0.01 ± 0.02	0.05 ± 0.06	0.04 ± 0.07
Z_{17}	-0.07 ± 0.09	0.05 ± 0.03	0.09 ± 0.02	0.06 ± 0.02	-0.07 ± 0.11
Z_{18}	0.11 ± 0.15	0.11 ± 0.05	0.11 ± 0.02	0.07 ± 0.05	-0.14 ± 0.05
Z_{19}	-0.06 ± 0.02	-0.07 ± 0.03	-0.10 ± 0.08	-0.07 ± 0.04	0.10 ± 0.03
Z_{20}	-0.06 ± 0.06	-0.24 ± 0.04	-0.17 ± 0.07	-0.05 ± 0.06	0.01 ± 0.11
Rms wave-front error					
($Z_1, Z_2 = 0$)	1.135	1.25	1.64	1.255	2.06
($Z_1-Z_5 = 0$)	0.337	0.45	0.42	0.5	0.99

^aExpressions and ordering of the Zernike polynomials are the same as in Ref. 21.

general, the highest variability is found for first-order, wave-front tilt terms, which measure the offset between the spot of the chief ray and the centroid of the whole spot diagram. Variability in first-order coefficients is mainly associated with experimental errors in the position of the chief ray that was taken as the origin of the coordinates from each run. Nevertheless, one can cancel these tilt terms by simply using the centroid of the spot diagrams as a new origin of coordinates. After the tilt terms, the highest coefficients correspond to the second-order polynomials, i.e., defocus (Z_4) and astigmatism (Z_3 and Z_5). This result is similar for all observers and for most eccentricities, consistent with previous findings.⁹ One interesting result is that many coefficients, among those having higher values [for instance, defocus (Z_4), astigmatism (Z_5), and coma (Z_7)], change from a negative (or positive) value at the fovea to have the opposite sign at 40°. This is a rather common feature for all observers, which suggests a plausible explanation for why the overall image quality varies gradually with eccentricity, despite individual coefficients, which show much higher variations. For most observers, it appears that foveal aberrations, caused by the lack of rotational symmetry at the fovea (astigmatism, coma, etc.), are helping to partially balance aberrations associated with high eccentricities, since both have the opposite sign. This would explain the relatively homogeneous image quality in the human eye,^{16,17} as compared with that of conventional optical systems.

Table 1 includes two bottom rows with the overall rms wave-front error for two cases. First, after canceling tilt terms ($Z_1, Z_2 = 0$), i.e., after centroiding the spot diagrams, and, second, after canceling both first- and second-order coefficients ($Z_1, \dots, Z_5 = 0$). The Strehl ratio has been estimated by computation of the ratio between the volume under the aberrated MTF (computed as the autocorrelation of the pupil function) and the volume under the aberration-free MTF. The Strehl ratio for observer EM ranges from 1.8% at 0° to 0.8% at 40° when all Zernike coefficients are considered and from 11.7% at 0° to 2.1% at 40° when first- and second-order terms are not considered. These low values of the Strehl ratio indicate, consistently with previous findings,¹⁶ that the eye is far from being a diffraction-limited optical system.

The overall rms wave-front distortion, averaged across the four observers, is shown in Fig. 4. The upper line (open circles) includes all Zernike terms, but as mentioned above, tilt terms (Z_1 and Z_2) are not especially meaningful because one can cancel them by simply placing the origin of the coordinates at the centroid of the spot diagram. The second line (filled diamonds) represents the rms error that remains after centroiding (making $Z_1 = Z_2 = 0$). If we also cancel defocus ($Z_4 = 0$), we get the open squares. Finally, the line with filled circles results after astigmatism is also canceled ($Z_3 = Z_5 = 0$). Error bars represent the standard deviation of the individual observers from the mean (they are not included in the second line so as to avoid overlap between the upper and the lower bars). At the fovea, defocus was the largest source of wave-front error (0.7 μm) for this particular set of observers, while astigmatism seems to have much less influence ($\sim 0.2 \mu\text{m}$). In a recent study by Liang and

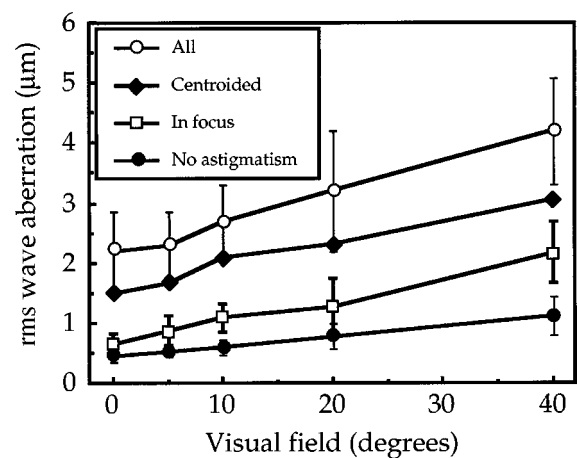


Fig. 4. Root-mean-square (rms) wave-front error averaged over our four observers. Error bars represent the standard deviation among observers. The four lines, from top to bottom, represent the mean when all Zernike terms are considered (open circles), when first-order terms are not considered (diamonds), when first-order terms and defocus are not considered (squares), and when first- and second-order terms are not considered (filled circles).

Williams⁹ on 14 eyes, it was found that the average contribution of astigmatism is 0.77 μm for a larger (7.3-mm) pupil, but this discrepancy seems to be due to the relatively large interobserver variability: The average amount of foveal astigmatism for their observers was 0.6 D but was only 0.4 D in our case. After astigmatism terms are subtracted, the remaining average rms wave-front error at the fovea is 0.45 μm , that is, 0.83 wavelength ($\lambda = 0.543 \mu\text{m}$). In addition, interobserver variability is significantly reduced as we remove first- and second-order Zernike terms. We can see the small error bars in the lowest line in Fig. 4. After first- and second-order coefficients are canceled, the rms error is similar among observers, despite the high interobserver variability found for each Zernike term.

Interestingly, the four lines in Fig. 4 show a roughly linear increment with eccentricity, which is much clearer in the lowest case (after removal of first- and second-order terms), for which the linear shape is manifest. Consequently, we can summarize the average results in a compact way, by estimating the average rate of increment of the rms wave-front error per degree of visual field. The resulting rates, obtained by least-squares fitting, are 0.052, 0.039, 0.037, and 0.017 $\mu\text{m}/\text{deg}$ for all coefficients after removal of terms for first order, first order and defocus, and first and second orders, respectively. These simple linear laws seem to be good enough to describe the average behavior found in our four observers, especially for the lowest line. However, it is important to bear in mind that these values are only a crude description of our average results, but individual eyes can show different behavior (for instance, the bottom row of Table 1 shows a rms that is lower than the mean at 0° but higher than the mean at 40°). Another question is, What line in Fig. 4 is the most representative of the eye's image quality? We can argue that centroiding is a rather easy task that has no effect on the shape of the PSF or the spot diagram, and

then we can neglect first-order terms. Thus the second line in the figure would be more representative than the first one. Following this kind of reasoning, we could say that we can focus the image with the help of trial lenses (canceling Z_4) and, finally, could compensate for astigmatism in the same way. However, in Fig. 5 we can see the change of defocus with visual field. Here the Sturm interval (dioptric range between the sagittal and the tangential foci) is represented by the bars, for observer EM, who presents the highest amount of astigmatism at the fovea. This figure helps to explain the elongated shape of the spot diagrams and PSF's for this observer: The top of the error bar is close to 0 at the fovea and is exactly 0 at 5° , which means that one of the Sturm foci is in focus. In general, defocus changes with eccentricity, so we can focus the image only for one visual angle at a time, and the same occurs with astigmatism. Actually, Fig. 5 displays the field curvature that represents the change of defocus and astigmatism (here represented only for EM) with eccentricity. Furthermore, the axis of astigmatism not

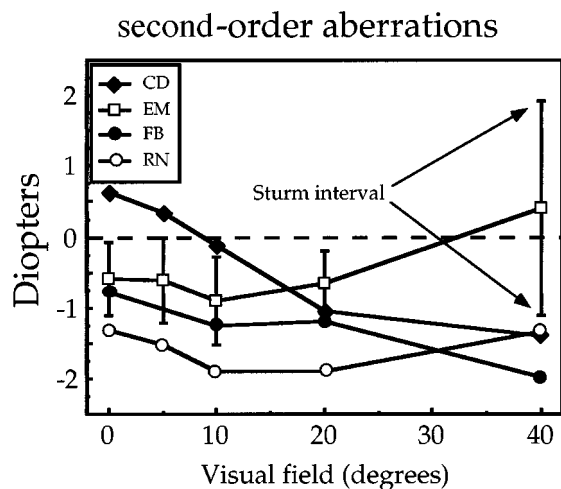


Fig. 5. Second-order aberrations in diopters for our four observers (defocus, field curvature, and astigmatism). The Sturm interval is represented by error bars for only one observer, for clarity.

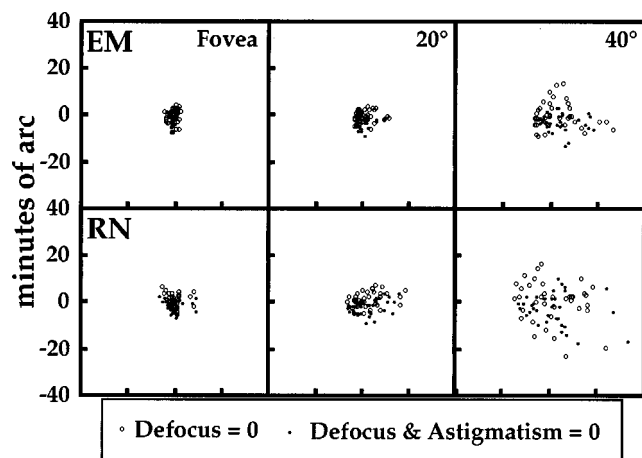


Fig. 6. Simulated spot diagrams that would be obtained after cancellation of defocus (open circles) and of both defocus and astigmatism (dots) with ideal trial lenses in two observers and three eccentricities.

only increases by also rotates with eccentricity. For observer EM it goes from -18° at the fovea to a maximum angle of $+38^\circ$ (at 20°). Thus, although it is easy to reach the lowest line of Fig. 4 by simple trial lenses (and it is even possible to go beyond this line with more sophisticated methods²⁶), doing so will, in general, introduce additional blur at other retinal locations. The spot diagrams that would result after exact correction of second-order aberrations are displayed in Fig. 6 for two observers and three eccentricities. The improvement is important in all cases and is remarkable for observer RN, mainly at the fovea, and is much less at 40° . However, one must bear in mind that in practice this exact correction cannot be made simultaneously at different eccentricities. Therefore, to have a realistic picture of the image quality of the eye across the visual field, one must consider second-order aberrations. In fact, a great deal of interobserver variability appears to be related to second-order terms, which is consistent with previous findings.¹¹⁻¹⁴

4. CONCLUSIONS

Geometrical aberrations across the visual field, measured objectively by a new laser ray-tracing technique on four naked eyes, are reported here. This is, to our knowledge, the first attempt to measure overall peripheral aberrations higher than second order (defocus, astigmatism, and field curvature). Aerial images corresponding to slightly blurred PSF's are highly correlated with geometrical spot diagrams, which constitutes experimental evidence supporting the validity of the ray-tracing method. Despite the large interobserver variability found in the aberration patterns (and in the PSF's), our four observers display a relatively homogeneous optical quality across the visual field. From these geometrical aberrations we have estimated the wave-front distortion by the standard method of fitting Zernike polynomials (fifth-order approximation), which again shows a large interobserver variability. The averaged (across our four observers) rms wave-front error, if we consider second-order and higher terms at the fovea, $1.49 \mu\text{m}$, increases roughly linearly up to $3 \mu\text{m}$ at 40° (mean rate of increase, $0.039 \mu\text{m}/\text{deg}$). If we do not consider second-order terms, both the rms error at the fovea, $0.45 \mu\text{m}$, and its mean increment, $0.017 \mu\text{m}/\text{deg}$, are significantly lower. In this case the overall rms error is surprisingly constant among observers, even though individual Zernike coefficients show a high variability among observers. Our results are consistent with the data reported in the literature on wave aberrations at the fovea, as well as on second-order peripheral aberrations, and could help to explain previous findings on peripheral modulation transfer functions and double-pass line-spread functions.

ACKNOWLEDGMENTS

This research was supported by the Spanish Comisión Interministerial de Ciencia y Tecnología (grant TIC97-0325).

REFERENCES

1. M. S. Smirnov, "Measurement of the wave aberration of the human eye," *Biofizika* **6**, 687–703 (1962) [*Biophysics (USSR)* **6**, 766–795 (1962)].
2. G. Van den Brink, "Measurements of the geometrical aberrations of the eye," *Vision Res.* **2**, 233–244 (1962).
3. M. C. W. Campbell, E. H. Harrison, and P. Simonet, "Psychophysical measurements of the blur on the retina due to optical aberrations of the eye," *Vision Res.* **30**, 1587–1602 (1990).
4. R. H. Webb, C. M. Penney, and K. P. Thompson, "Measurement of ocular local wavefront distortion with a spatially resolved refractometer," *Appl. Opt.* **31**, 3678–3686 (1992).
5. H. C. Howland and B. Howland, "A subjective method for the measurement of monochromatic aberrations of the eye," *J. Opt. Soc. Am.* **67**, 1508–1518 (1977).
6. F. Berny, "Etude de la formation des images retiniennes et determination de l'aberration de sphericite de l'oeil humain," *Vision Res.* **9**, 977–990 (1969).
7. G. Walsh, W. N. Charman, and H. C. Howland, "Objective technique for the determination of monochromatic aberrations of the human eye," *J. Opt. Soc. Am. A* **1**, 987–992 (1984).
8. J. Liang, B. Grimm, S. Goelz, and J. F. Bille, "Objective measurement of wave aberrations of the human eye with the use of a Hartmann–Shack wave-front sensor," *J. Opt. Soc. Am. A* **11**, 1949–1957 (1994).
9. J. Liang and D. R. Williams, "Aberrations and retinal image quality of the normal human eye," *J. Opt. Soc. Am. A* **14**, 2873–2883 (1997).
10. R. Navarro and M. A. Losada, "Aberrations and relative efficiency of ray pencils in the living human eye," *Optom. Vision Sci.* **74**, 540–547 (1997).
11. C. E. Ferree, G. Rand, and C. Hardy, "Refraction for the peripheral field of vision," *Arch. Ophthalmol.* **5**, 717–731 (1931).
12. F. Rempt, J. Hoogerheide, and W. P. H. Hoogenboom, "Peripheral retinoscopy and the skiagram," *Ophthalmologica* **162**, 1–10 (1971).
13. M. Millodot and A. Lamont, "Refraction of the periphery of the eye," *J. Opt. Soc. Am.* **64**, 110–111 (1974).
14. G. Smith, M. Millodot, and N. McBrien, "The effect of accommodation on oblique astigmatism and field curvature of the human eye," *Clin. Exp. Optom.* **71**, 119–125 (1988).
15. J. A. M. Jennings and W. N. Charman, "Off-axis image quality in the human eye," *Vision Res.* **21**, 445–455 (1981).
16. R. Navarro, P. Artal, and D. R. Williams, "Modulation transfer of the human eye as a function of retinal eccentricity," *J. Opt. Soc. Am. A* **10**, 201–212 (1993).
17. D. R. Williams, P. Artal, R. Navarro, M. J. McMahan, and D. H. Brainard, "Off-axis optical quality and retinal sampling in the human eye," *Vision Res.* **36**, 1103–1114 (1996).
18. S. Fisher, "Contour plots and the limit of 'clear and comfortable vision' in the near zone of progressive addition lenses," in *Vision Science and Its Applications*, Vol. 1 of 1997 OSA Technical Digest Series (Optical Society of America, Washington, D.C., 1997), pp. 2–5.
19. D. Sliney and M. Wolbarsht, *Safety with Lasers and Other Optical Sources*, 1st ed. (Plenum, New York, 1980).
20. R. A. Moses, ed., *Adler's Physiology of the Eye: Clinical Application* (Mosby, St. Louis, Mo., 1981), p. 747.
21. D. Malacara, *Optical Shop Testing*, 2nd ed. (Wiley, New York, 1992).
22. M. C. Rynders, R. Navarro, and M. A. Losada, "Objective measurement of the off-axis longitudinal chromatic aberration in the human eye," *Vision Res.* **37**, 513–521 (1997).
23. M. Born and E. Wolf, *Principles of Optics*, 5th ed. (Pergamon, Oxford, 1975).
24. R. Navarro and M. A. Losada, "Phase transfer and point-spread function of the human eye determined by a new asymmetric double-pass method," *J. Opt. Soc. Am. A* **12**, 2385–2392 (1995).
25. R. Navarro and M. A. Losada, "Shape of stars and optical quality of the human eye," *J. Opt. Soc. Am. A* **14**, 353–359 (1997).
26. J. Liang, D. R. Williams, and D. T. Miller, "Supernormal vision and high-resolution retinal imaging through adaptive optics," *J. Opt. Soc. Am. A* **14**, 2884–2892 (1997).